# Silicon-integrated photonic circuit for a single-stage large-angle beam steering optical phased array

David Kwong, Yazhao Liu, Amir Hosseini, Yang Zhang, Beomsuk Lee, Cheyun Lin, and Ray T. Chen

Microelectronic Research Center, Department of Electrical and Computer Engineering, University of Texas, Austin, TX 78758 USA (e-mail: diddykwong@gmail.com; liuyazhao@mer.utexas.edu; chen@ece.utexas.edu)

## ABSTRACT

In this paper, we present the results of the design and fabrication of a 12 channel nano-membrane-based optical phased array that allows for large angle beam steering operating at wavelength=1.55μm. Our device is fabricated on silicon-on-insulator using standard CMOS process. By implementing unequally spaced waveguide array elements, we can relax the half-wavelength spacing requirement for large angle beam steering, thereby avoiding the optical coupling between adjacent waveguides and reducing the side-lobe-level of the array radiation pattern. 1D beam steering of tranverse-electric polarized single mode light is designed to be achieved thermo-optically through the use of thin film metal phase shifters.

**Keywords:** beam steering, nanomembrane, thermo-optic, phased array, silicon-on-insulator

## 1. INTRODUCTION

Phased-array antennas are expected to be effectively utilized in modern radar and communication systems. These systems cover frequencies commonly used for military imaging, such as ground penetrating radar, through-wall imaging, security, and medical imaging [1]. Phased-array antennas offer many advantages including mechanical-free steering, increased scan flexibility in two dimensions, precise elemental phase and amplitude control, and the potential for large peak and average power. Recently, optically controlled phased-array antennas have become much more attractive due to their simplicity by substituting a number of microwave components for simple optics, as well as their high speed, compact and lightweight size, and ease of integration with other state-of-the-art instruments in optical communication. Various kinds of research on the optical control of array antennas have been encouraged by various organizations [2]–[5], such as photonic radio-frequency (RF) phase shifters [6]–[11], and several optical beam forming architectures proposed by other research groups [12]–[23].

There are two main approaches to optically controlled phased-array antennas. True time delay (TTD) systems [12]–[16] provide large bandwidth but usually require long free-space sections that imply inevitable diffraction and loss issues. Phase control systems [17] exploit the parallelism of free-space and so are normally more compact, which can be a promising feature for optical integrated circuits in the future. A variety of OPA devices based on phase control have been experimentally demonstrated. Micro-electroptical systems (MEOS) are the first generation concept due to their similarity to MEMS. However, the sizes of MEOS devices are the main concern. An optical fiber array arranges the optical fibers in two dimensions and shrinks the size to a certain extent, but cannot satisfy the strict requirement for highly compact integrated optical circuits. In order to miniaturize and mechanically stabilize, OPA on optical waveguides has been found to be effective [24], [25]. An optical waveguide array can greatly reduce the size of the optical processing part, optical alignment difficulties, and optical insertion losses.

In this paper we present a highly integrated beam steering system based on an OPA on silicon-on-insulator (SOI). The active size of this device is only about 1 mm. We achieved good results for both the near field and far field imaging. The line shape of the far field signal can be further used in optical beam scanning.

# 2. DEVICE DESIGN AND OPERATION

Our device consists of two layers; the first layer contains the passive optical circuit and the second layer is composed of the thermo-optic active phase shifters. These two layers are separated by an oxide cladding layer to prevent loss that would occur from the penetration of the evanescent electromagnetic tail into the metal phase shifter, as shown in Figure 1(a). Figure 1(b) shows the optical circuit which consists of the multi-mode interference (MMI) splitter, the s-bend waveguides, and the unequally spaced OPA itself. We have simulated the performance of such an OPA fabricated on SOI wafer theoretically [29]. This OPA is fed by a MMI coupler that splits the input signal instead of the free space propagation section used in conventional arrayed waveguide gratings.
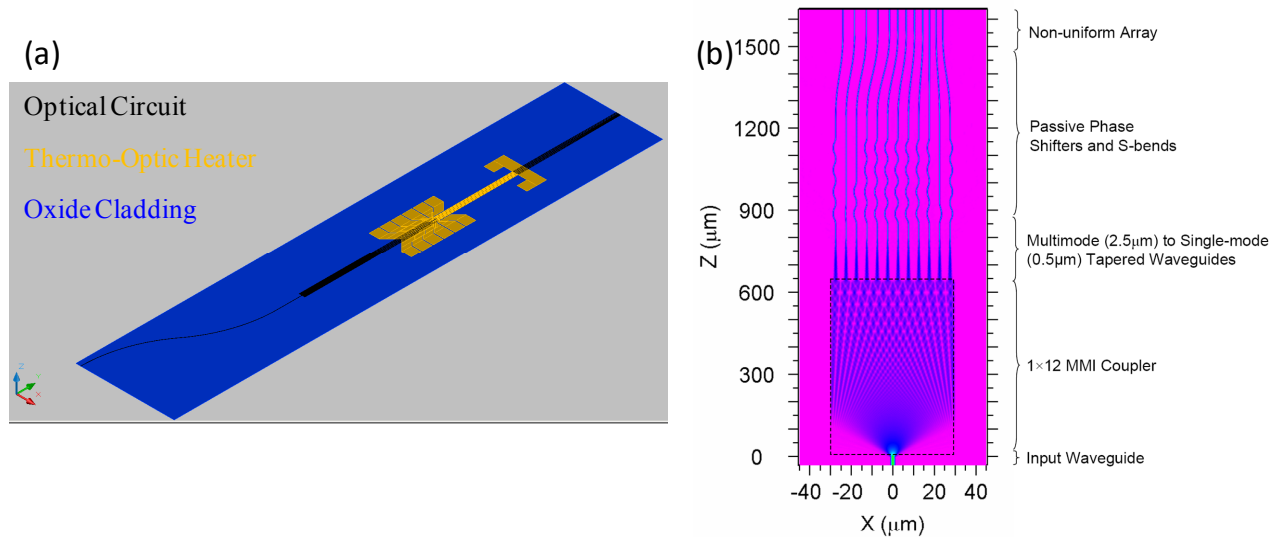
Figure 1 (a) Layout of full device and (b) optical circuit layout and components

## 2.1 Design and Optimization of MMI

Multi-mode interference couplers are widely used in photonic integrated circuits (PICs) as power splitters, optical switches, and for other signal routing processes [29]. This is due to the significant advantages that MMI couplers provide through their compact size, low loss, stable splitting ratio, low crosstalk, and imbalance, large optical bandwidth, insensitivity to polarization, ease of production, and good fabrication tolerances [28]. As one of the largest uses of MMI couplers is for power splitters, the power distribution at the output ports has been thoroughly investigated. However, very little is understood about the phase profile at the MMI output, but this knowledge is important in beam steering applications because it determines the amount of active phase shift required. We have derived an analytical closed loop expression for the phase shift at each of the output ports for a 1-by-N MMI coupler [30]. Here we briefly introduce our findings for the sake of completeness.

MMI couplers operate based on the phenomenon of self-imaging in multi-mode waveguides, whereby an input field profile is reproduced in single or multiple images at periodic intervals along the propagation direction of the guide [30]. From figure 1, the multimode waveguide consists of a core with refractive index $n_c$ and width $W$, and has N output ports. The multimode section can support a maximum of N+1 modes. For each mode $p$, the dispersion relation is given as

$$\beta_p^2 + \kappa_{yp}^2 = \left(\frac{2\pi n_c}{\lambda_0}\right)^2, \tag{1}$$

where, $\beta_p$ is the propagation constant of the the pth mode, $\lambda_0$ is a free-space wavelength. $\kappa_{yp}$ is the lateral wavenumber of the pth mode, given as $\kappa_{yp} = (p+1)\pi/W_e$, where $W_e$ is the effective width for mode m including the penetration depth due to the Goose-Hahnchen shift [2]. The propagation constant $\beta_p$ can be approximated as

$$\beta_p \approx \beta_0 - \frac{p(p-2)}{3L_\pi},\tag{2}$$

where, $L_\pi = \pi/(\beta_0 - \beta_1) \approx 4n_c W_e^2/3\lambda_0$. Furthermore, each mode accumulates phase according to its own propagation constant, and the field profile at z=L can be written as

$$\exp(-j\beta_0 L)\sum_{p=0}^{M} c_p \phi_p(y)\exp\left(-j(\beta_p - \beta_0)L\right) \approx$$

$$\exp(-j\beta_0 L)\sum_{p=0}^{M} c_p \phi_p(y)\exp\left(j\frac{p(p+2)\pi}{3L_\pi}L\right).\tag{3}$$

At $L = 3rL_\pi$ with $r = 1, 2, ...$, all the exponential terms in the previous equation become in-phase with one another and a single image of the input field profile is formed. Generally, an N-fold image of the input field profile is formed at $L = 3L_\pi/N$. However, by using a symmetric input fed to the center of the multi-mode waveguide, a 4X reduction in the required length of the coupler can be achieved, so that $L = 3rL_\pi/4N$ [28].

For 1-by-N couplers, ideally the ouput power is to be divided equally among the output ports, and thus the field amplitude should be $1/\sqrt{N}$. However, the approximation for the propagation constant $\beta_p$ becomes inaccurate in reality, especially for the higher order modes in low-refractive-index contrast waveguides. This results in an error in the accumulated phase shift of each mode. These modal phase errors are the main cause of non-uniformity in the ouput field amplitudes and output intensity. These errors are more pronounced in low-refractive index contrast waveguides, such as a MMI made of the polymer ZPU12-RI which has a low refractive index contrast [28], and can be seen in Figure 2(b). To avoid this error, we use silicon as our core material, which can provide good confinement for the electric field at $\lambda = 1.55\mu m$.
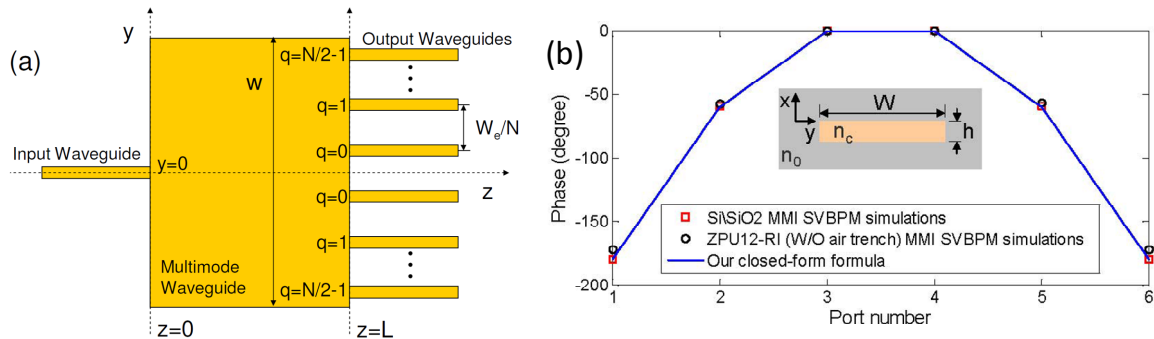


Figure 2 (a) Schematic of a 1-by-N symmetric MMI coupler for even N. (b) Output phase profile of a 6 port MMI coupler comparing the analytical closed form formula, a Si/SiO2 simulation, and a low index polymer ZPU12-RI MMI.

## 2.2 Design and Optimization of Unequally Spaced OPA

Optical phased arrays are simply arrays of single-mode waveguides operating at the designated wavelength. Beam steering can be achieved by modulating the phase shift of each waveguide element in the array. To achieve wide steering angles in a uniform array, the waveguide spacing must be reduced to half the wavelength but this result in optical coupling between adjacent waveguides which causes far field pattern distortion. This has the effect of increasing the side lobe level and thus reducing the power and steering efficiency [29]. A solution is to use an unequally spaced OPA that can relax this half-wavelength requirement. We have previously proposed a design methodology that provides both large angle steering while minimizing the side lobe level caused by optical cross-talk [31].

Our non-uniform array is realized by placing sub-arrays of equally spaced arrays next to each other, as can be seen in Figure 3(b). Our design methodology is as follows and uses the following definitions:
- N=total number of array elements

- M=number of sub-arrays
- $s_i$=spacing in sub-array i, for i=1,2,3…
- $s_i = q_i s_0$
  - $s_0 = \lambda/2$
  - $q_i$ is the smallest integer such that the $\gcd(q_i, q_j) = 1$ where $i \neq j$

It is important to note that $s_0$ must be less than $\lambda/2$ so that sub-array grating lobes will not overlap. With this design methodology, the main lobes of each sub-array add up constructively, while there is no overlap between the grating lobes of each sub-array [29]. Our implementation of this design is an array with N=12 elements, which is comprised of M=3 subgroups each with 4 equally spaced elements. The array spacing is as follows:
- $\lambda = 1.6\mu m$ and $s_0 = 0.8\mu m$
- $q_1 = 4$, $q_2 = 5$, $q_3 = 7$, and $s_1 = 3.2\mu m$, $s_2 = 4\mu m$, $s_3 = 5.6\mu m$.
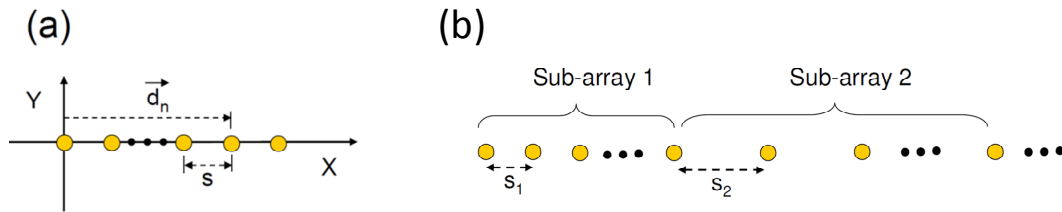


Figure 3-Equally spaced array (a) and unequally spaced array composed of equally spaced sub-arrays (b).

## 2.3 Phase Shifting

We desire to have an output beam that comes out straight, that is, at 0° steering, without any active phase shifting. To achieve this, it is necessary to equalize the phase of each output port by equalizing the optical path length with the use of additional s-bends. These s-bend segments serve the dual purposes of converting the equally spaced MMI output to the unequally spaced OPA, while at the same time passively equalizing the phase shifts at each of the MMI output ports.

Active phase shifting is achieved via the use of thermo-optic metal heaters that will utilize silicon's strong thermo-optic coefficient to modulate the refractive index and thereby the accumulated phase at the output of each array element. Our heater is essentially a metal wire whose temperature can be adjusted by changing the current through it. The heater is placed above the waveguide and is separated from the waveguide by a sufficiently thick oxide cladding layer to prevent optical absorption loss from the conductive metal.

In our design we have opted to make the heaters independently controllable; that is, we have (N+1) electrodes to provide for 12 heaters along with a common ground. This provides us the significant advantage of being able to reset after each $2\pi$ phase shift. Had we opted to simplify this electrical design by having only two electrodes, there would be no reset and thus the phase shift required at the end of the array would be impractical to achieve.

We have chosen the length of the heater region to be 800 μm and determined the necessary temperature change in the waveguide according to the equation below.

$$\Delta\phi = \frac{2\pi}{\lambda}\left(\frac{dn}{dT}\right)_{Si} \cdot \Delta T \cdot L_H \tag{4}$$

Where $\Delta\varphi$ is the desired phase shift of $2\pi$, $\lambda$ is the wavelength of light (1550nm), dn/dT is the thermo-optic coefficient of silicon (1.86E-4), $\Delta T$ is the temperature change in the waveguide, and $L_H$ is the length of the heater. Thus, we need to raise the temperature of the silicon waveguide by 10.4 degrees.

Figure 4 shows the schematic layer structure of the heater, along with a transient simulation of the response time to achieve the $2\pi$ phase shift.
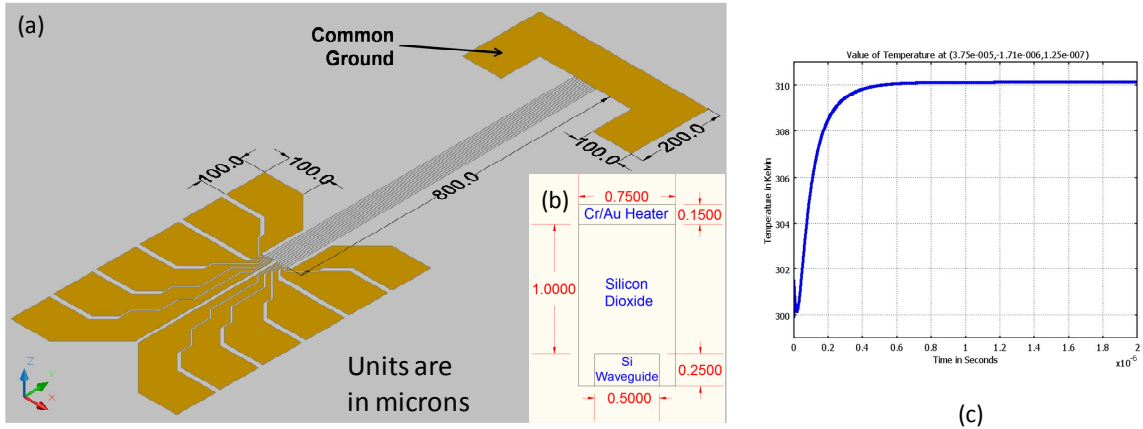
Figure 4-Schematic of thermo-optic heater structure (a), along with cross section view (b). Transient simulation showing the response time to raise the silicon waveguide to reach the temperature for $2\pi$ phase shift (c).

## 3. DEVICE FABRICATION

Our device is implemented on silicon on insulator (SOI) for a variety of reasons. Silicon CMOS process technology is mature and can be easily adopted here. Also, silicon has a large thermo-optic coefficient that provides for ease of fabrication while still demonstrating large-angle beam steering with acceptable speed. Furthermore, we can utilize the large refractive index difference between silicon and silicon dioxide to minimize the modal phase errors and hence the non-uniformity in the output intensity, while at the same time achieving good modal confinement.

The unequally spaced optical phased array with thermo-optic metal heaters were fabricated on SOI from SOITEC with 3 μm buried oxide layer (BOX) and 260 nm top silicon layer. The optical circuit was patterned using a JEOL JBX600 electron beam lithography system, as shown in Figure 5. The pattern was inverted by using a titanium liftoff step, and subsequently transferred to the top silicon layer via reactive ion etching (RIE) and piranha cleaning. Afterwards, a 1 μm film of plasma-enhanced chemical vapor deposition (PECVD) silicon dioxide was deposited for the top cladding using the Plasmatherm 790 system. The refractive index was found to be $n_{PECVD}$=1.46. Afterwards, thermo-optic heaters were formed on top of the oxide cladding using photolithography and subsequent deposition and liftoff of a 150nm Cr/Au film, as shown in Figure 6(a).
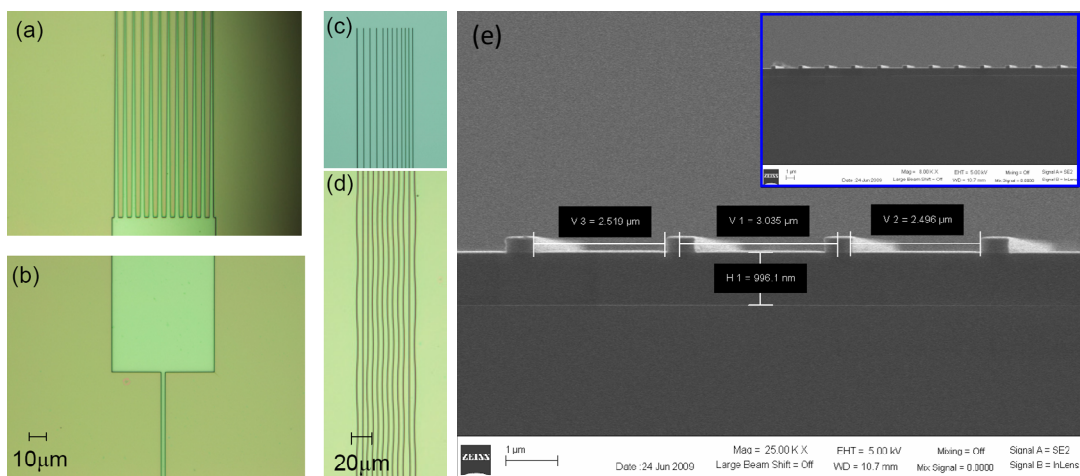


Figure 5-Optical scope picture of optical circuit showing (a) the MMI output and tapered waveguides, (b) the input waveguide to the MMI coupler, (c) the unequally spaced OPA output, (d) the s-bend regions and (e) VSEM image of OPA output.

After the device was completed, the device was cleaved to provide optical input and output and mounted on a chip carrier that was then wire-bonded to provide electrical connections for the thermo-optic phase shifters. Our chip carrier was fabricated on copper printed circuit board (PCB) that was patterned to provide an interface between our power generator and metal heaters, seen in Figure 6(b).
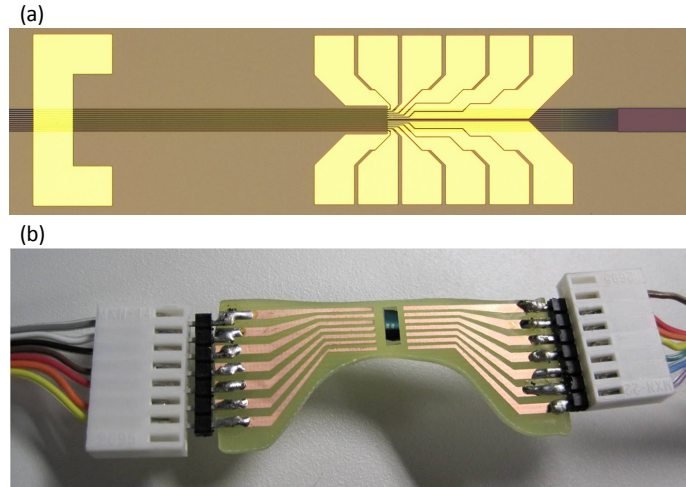


Figure 6-(a) Optical scope picture of the completed device showing the metal heater over the waveguides after the MMI output. (b) - Photograph of a cleaved sample mounted onto a chip carrier and attached to the power generator.

## 4. RESULTS AND ANALYSIS

The performance of our OPA was measured using the experimental setup shown in Fig.7.
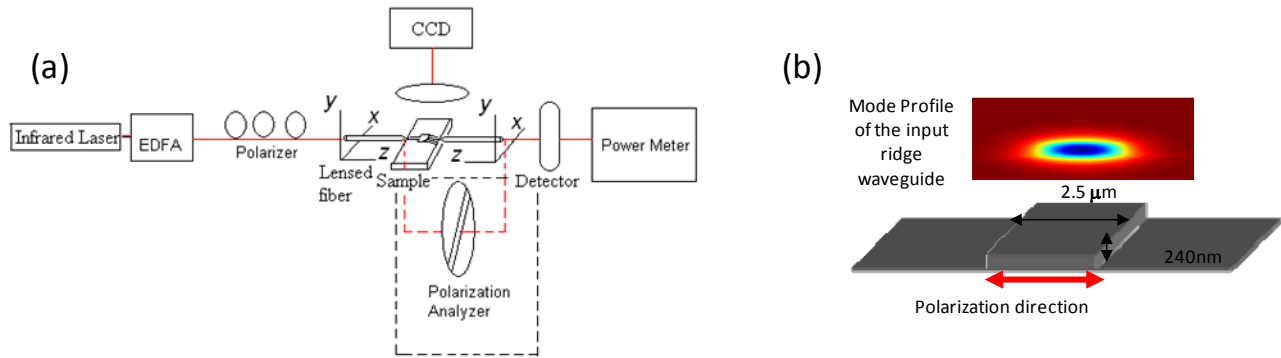


Figure 7-(a) Optical Test Setup and (b) mode profile of input ridge waveguide.

In the optical source part, a tunable polarized semiconductor laser operating at a wavelength range from 1520-1620nm was used as the input light source. The input signal from the infrared laser was amplified by a polarization maintaining EDFA working in the C+L band. A filter combined polarizer was used to provide TE polarization for the input signal. A polarization analyzer was also used to confirm the polarization state in the whole system. We used a visible and infrared light dual imaging system to monitor the photon transmission in the whole OPA system. The monitor system was set directly above the OPA device. It included a high magnification rate objective lens 100X as well as a broad band CCD camera sensitive to light with wavelength 400nm-2µm.

For the optical connection to the OPA devices, the fiber was aligned to the input waveguide of OPA device precisely via a six-axis automated aligner to achieve a precision in movement of 50nm. For the near field image detection, a polarization maintaining fiber (PMF) and single mode fiber (SMF) have been connected to the input and output facets, respectively. Both input and output fibers are non-imaging lensed fibers with a mode field diameter of 2.5 micron, to make the mode field of the input fiber coincide well with that of the rib waveguide. The signal from each output channel was collected by the output SMF, and then was fed to an InGaAs photodetector, where the optical signal was transferred to an electrical signal before being sent to the power meter. Finally, we connected the power meter to the PC by a signal acquisition system, which feeds back to the auto aligner to control the position of the input and output fibers to maintain optimal coupling.

During our experiments, we adjusted the input fiber in three dimensions precisely and use the dual imaging CCD system to monitor the coupling. Because our OPA devices were fabricated on SOI wafer and thus provides for good light confinement in the silicon core, we were able to observe the light transmission in the rib waveguides and OPA from the TV screen at the best coupling position. Figure 8 shows the coupling process observed from the monitor system. With an illuminator, visible light imaging helped us to locate the working area in OPA. Infrared light imaging detection gave the exact signal information. Figure 8(a) is the 12 output channels under visible light, and Figure 8(b) is the corresponding infrared image. 12 bright spots caused by the light scattering into the vertical dimension were clearly seen from the screen.

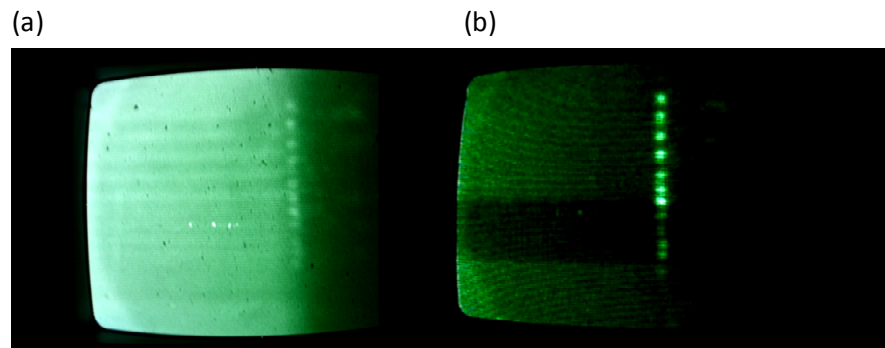(a)                                             (b)



Figure 8 Top down microscope image of the 12 output channels using (a) visible light and (b) infrared light when light is coupled into the device.

After verifying the coupling position, we aligned the output SMF to the output side of the OPA device. Since the output channel of the OPA is only 500nm in width, the coupling position between the waveguide and fibers needed to be adjusted accurately. We kept the input fiber fix at the best coupling position, and scanned the output fiber in a rectangular region with a size of 70 x 5 $\mu m^2$, which was large enough to cover the OPA near-field output region. The optical signal collected by the SMF was transmitted to the power meter and fed to the data acquisition system in PC. This data is stored as a 2D matrix, with each entry representing the optical power intensity at the corresponding spatial location. The scanning results are shown in Figure 9(a) which is in agreement with the simulated intensity distribution in Figure 9(b). The results are also tabulated and compared to the device structure in Table I. The dual monitor system and the fiber collection system confirmed each other successfully.
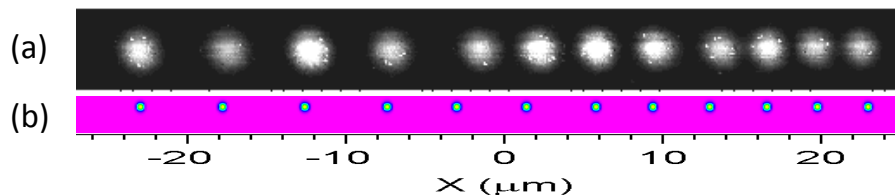


Figure 9 Experimental output intensity of each of the 12 output channels as scanned by lensed fiber at output (a) and simulated output intensity distribution (b).

Table I Output intensity and position of each of the 12 output channels as scanned by lensed fiber at output.

| | Power Intensity (dBm) | Distance from neighboring channel (μm) | Distance from neighboring power peak (μm) | Total scale of channels (μm) | Total scale of peaks (μm) |
|---|---|---|---|---|---|
| Channel 1 | -19.95 | | | | |
| Channel 2 | -21.09 | 5.6 | 5.8 | | |
| Channel 3 | -17.79 | 5.6 | 5.4 | | |
| Channel 4 | -20.73 | 5.6 | 5.6 | | |
| Channel 5 | -20.51 | 5.6 | 5.8 | | |
| Channel 6 | -18.54 | 4.0 | 3.9 | | |
| Channel 7 | -18.03 | 4.0 | 3.8 | 48 | 47.8 |
| Channel 8 | -18.71 | 4.0 | 4.0 | | |
| Channel 9 | -20.79 | 4.0 | 4.4 | | |
| Channel 10 | -19.68 | 3.2 | 3.2 | | |
| Channel 11 | -21.27 | 3.2 | 3.3 | | |
| Channel 12 | -21.80 | 3.2 | 2.6 | | |

The results of the fiber-to-fiber loss were measured on the packaged module. The input power was 10mW. The total throughput for the output signal in each channel is approximately 50 dB. 16 dB of the observed fiber-to-fiber throughput of 50 dB is due to the polarization mismatch and insertion loss between the fiber connectors. 17-27 dB (dependent on cleaving) comes from the fiber-chip coupling losses, which could be largely overcome by using suitable anti-reflective (AR) coated fiber, and the measurements also include the loss (4 dB) due to polarization control, which was provided by a non-contacted filter combined polarizer, thus the actual fiber-to-fiber transmission loss is less than 10 dB.

For the far field signal detection, we used an infrared (IR) display card instead of the single-mode lensed fiber. Light from the 12 output channels undergo interference to produce the far field pattern, and forms a straight line extended in the vertical dimension, as shown in Figure 10(a). This can be compared with the simulated far field pattern in Figure 10(b). Using the thermo-optic heater for phase modulation can produce beam steering in the horizontal direction with low side love level and high tolerances in power fluctuation, which will be discussed in a separate paper.
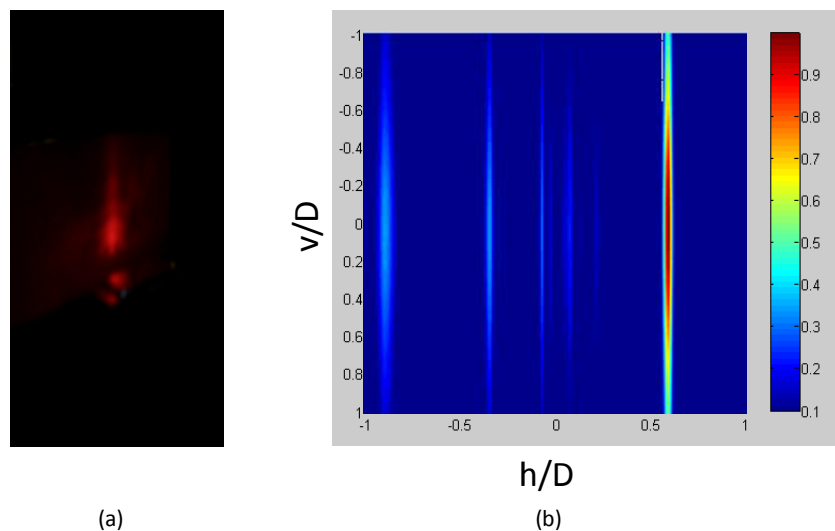


(a)        (b)

Figure 10 (a) Far field pattern seen on IR detector card and (b) simulated far field pattern.

# 5. CONCLUSION

In conclusion, we present the design and fabrication of a highly integrated beam steering system. Using the designed MMI and unequally spaced OPA, we are able to achieve both the near-field and far-field images, which are in good agreement with our theoretical analysis. The beam steering system we provided in this paper has good potential utilization in optical communication and detection. Using nanomembrane transfer and stacking techniques, one can achieve large angle beam steering in two dimensions.

# 6. ACKNOLWEDGEMENTS

# REFERENCES

[1] "Ultra-wideband transmission systems, first report and order," FCC, Washington, DC, FCC 02-48, Apr. 2002.

[2] N. Riza, Ed., Selected Papers on Photonic Control Systems for Phased Array Antenna. ser. SPIE Milestone. Bellingham,WA: SPIE Opt. Eng. Press, 1997, vol. MS 136.

[3] Kumar, Antenna Design with Fiber Optics. Norwood, MA: Artech House, 1996.

[4] Beamforming techniques for active phased array antenna based communication satellites. presented at 1999 IEEE MTT-S Int. Microwave Symp. Workshop

[5] P. J. Matthews, "Practical photonic beamforming," in Int. Microwave Photon. Topical Meeting, 1999, pp. 271–274,.

[6] D. K. Paul, "Optical beam-forming and steering for phased-array antenna," in Proc. IEEE Natural Telesys. Conf., June 1993, pp. 7–12.

[7] Y. Kamiya, W. Chujo, K. Yasukawa, K. Matsumoto, M. Izutsu, and T. Sueta, "Fiber optic array antenna using optical waveguide structure," in IEEE Int. Symp. Dig. Antennas Propagation, vol. 2072, May 1990, pp. 774–777.

[8] J. F. Coward, T. K. Yee, C. H. Chalfant, and P. H. Chang, "A photonic integrated- optic RF phase shifter for phased array antenna beam-forming application," J. Lightwave Technol., vol. 11, pp. 2201–2205, Dec 1993.

[9] D. Jez, K. Cearns, and P. Jessop, "Optical waveguide components for beam forming in phased-array antennas," Microwave Optical Technol. Lett., vol. 15, no. 1, pp. 46–49, 1997.

[10] J. M. Fuster, J. Marti, J. L. Corral, and P. Candelas, "Harmonic up/downconversion through photonic RF phase shifters in phased-array antenna beam-forming applications," Microwave Optical Technol. Lett., vol. 22, no. 4, pp. 247–249, Aug. 1999.

[11] S. R. Henion and P. A. Schulz, "Electrooptic phased array transmitter," IEEE Photon. Technol. Lett., vol. 10, pp. 424–426, Mar. 1998.

[12] R. D. Esman, M. Y. Frankel, J. L. Dexter, L. Goldberg, and M. G. Parent, "Fiber optic prism true time delay antenna feed," IEEE Photon. Technol. Lett., vol. 5, pp. 1347–1349, Nov. 1993.

[13] B. Vidal, J. L. Corral, M. A. Piqueras, and J. Martí, "Optical delay line based on arrayed waveguide gratings' spectral periodicity and dispersive media for antenna beamforming applications," IEEE J. Sel. Topics Quantum Electron., vol. 8, pp. 1202–1210, Nov./Dec. 2002.

[14] B. Vidal, J. L. Corral, and J. Martí, "Optical delay line employing an arrayed waveguide grating in fold-back configuration," IEEE Microw. Wireless Compon. Lett., vol. 13, pp. 238–240, Jul. 2003.

[15] D. T. K. Tong and M. C.Wu, "A novel multiwavelength optically controlled phased array antenna with a programmable dispersion matrix," IEEE Photon. Technol. Lett., vol. 8, pp. 812–814, Jun. 1996.

[16] M. A. Piqueras, G. Grosskopf, B. Vidal, J. Herrera, P. Sanchis, V. Polo, J. L. Corral, A. Marceaux, J. Galière, J. Lopez, A. Enard, J. L. Valard, O. Parillaud, E. Estèbe, N. Vodjdani, J. H. d. Besten, F. Soares, M. K. Smit, and J. Marti, "Optically beam formed beam switched adaptive antennas for fixed and mobile broadband wireless access networks," IEEE Trans. Microw. Theory Tech., vol. 54, pp. 887–899, Feb. 2006.

[17] N. A. Riza, S. A. Khan, and M. A. Arain, "Flexible beamforming for optically controlled phased array antenna," Opt. Commun., vol. 227, pp. 301–310, Sep. 2003.

[18] D. Dolfi, F.Michel-Gabriel, S. Bann, and J. P. Huignard, "Two-dimensional optical architecture for time-delay beam forming in a phased array antenna," Opt. Lett., vol. 16, pp. 225–257, Feb. 1991.

[19] Project OBEFONE: Technologies for Optical Payloads ESA-SENER TRP EE-010.

[20] F. Dalmases, S. Blanch, J. Romeu, L. Jofre, B. Vidal, J. Marti, I. Mackenzie, E. Vez, and J. Santamaria, "Optically beam formed array performance," in Eur. Conf. on Antennas and Propagation, EuCAP, Nice, France, Nov. 6–11, 2006.

[21] F. Dalmases, S. Blanch, J. Romeu, L. Jofre, B. Vidal, J. Marti, I. Mackenzie, E. Vez, and J. Santamaria, "Wideband optical TTD SAR antenna," in IEEE Mediterranean Electrotechnical Conf.—Melecon, Malaga, Spain, May 16–19, , pp. 336–339.

[22] B. Vidal, T. Mengual, C. Ibáñez-López, and J. Martí, "Optical beamforming network based on fiber optical delay lines and spatial light modulators for large antenna arrays," IEEE Photon. Technol. Lett., vol. 18, no. 24, pp. 2590–2592, Dec. 2006.

[23] T. Mengual, B. Vidal, C. Stoltidou, S. Blanch, J. Marti, L. Jofre, I. McKenzie, and J. M. del Cura, "Optical phase-based beamformer using MZM SSB modulation combined with crystal polarization optics and a spatial light modulator," Optics Communications, accepted for publication.

[24] I. Ogawa, K. Horikawa, T. Kitoh, and H. Ogawa, "Novel multibeam forming network miniaturized by optical slab waveguide," in Proc. Int. Antenna Propagat. Symp., 1996, pp. 121–124.

[25] T. Akiyama, K. Inagaki, Y. Mizuguchi, and T. Ohira, "Multibeam optical signal processing array antenna using optical waveguide arrays and lens," Trans. IEICE, vol. E84-B, pp. 2413–2420, Sept. 2001.

[26] Rajarajan, M.; Rahman, B.M.A.; Wongcharoen, T.; Grattan, K.T.V., "Accurate analysis of MMI devices with two-dimensional confinement ," *Lightwave Technology, Journal of* , vol.14, no.9, pp.2078-2084, Sep 1996

[27] Wang, Xialong; Chen, Ray T.; "Image enhanced polymer-based multimode interference coupler covering C and L bands using deeply etched air trenches," Appl. Phys. Lett. 90, 111106 (2007),

[28] Amir Hosseini, David N. Kwong, Che-Yun Lin, Beom Suk Lee, and Ray T. Chen, Output Formulation for Symmetrically-Excited one-to-N Multimode Interference Coupler, IEEE Journal of selected topics in quantum electronics, to appear (2010)

[29] Amir Hosseini, David N Kwong, and Ray T. Chen, Wide steering angle optical phased array based on silicon nano-membrane, Proc. SPIE 7221, 72210T (2009)

[30] L. Soldano and E. Pennings, "Optical multi-mode interference devices based on self-imaging: Principles and applications," *J. Lightw. Technol.*, vol. 13, no. 4, pp. 615–627, Apr. 1995.

[31] Feng Xiao, Weiwei Hu, and Anshi Xu, "Optical phased-array beam steering controlled by wavelength," Appl. Opt. 44, 5429-5433 (2005)

[32] J. H. Abeles and R. J. Deri, "Suppression of sidelobes in the far-field radiation patterns of optical waveguide arrays" Appl. Phys. Lett. 53, 1375 (1988)